Colossal Room-Temperature Electrocaloric Effect in Ferroelectric Polymer Nanocomposites Using Nanostructured Barium Strontium Titanates

Guangzu Zhang,[†,‡,#] Xiaoshan Zhang,[†,§,#] Tiannan Yang,[†] Qi Li,[†] Long-Qing Chen,[†] Shenglin Jiang,[*,‡] and Qing Wang[*,†]

[†]Department of Materials Science and Engineering, The Pennsylvania State University, University Park, Pennsylvania 16802, United States, [‡]School of Optical and Electronic Information, Huazhong University of Science and Technology, Wuhan, Hubei 430074, China, and [§]College of Materials Science and Engineering, Sichuan University, Chengdu 610064, China. [#]G. Zhang and X. Zhang contributed equally to this work.

ABSTRACT The electrocaloric effect (ECE) refers to conversion of thermal to electrical energy of polarizable materials and could form the basis for the next-generation refrigeration and power technologies that are highly efficient and environmentally friendly. Ferroelectric materials such as ceramic and polymer films exhibit large ECEs, but each of these monolithic materials has its own limitations for practical cooling applications. In this work, nanosized barium strontium titanates with systematically varied morphologies have been prepared to form polymer nanocomposites with the ferroelectric polymer matrix. The solution-processed polymer nanocomposites exhibit an extraordinary room-temperature ECE *via* the synergistic combination of the high breakdown strength of a ferroelectric polymer matrix and the large change of polarization with temperature of ceramic nanofillers. It is found that a sizable ECE can be generated under both modest and high electric fields, and further enhanced greatly by tailoring the morphology of the ferroelectric nanofillers such as increasing the aspect ratio of the nanoinclusions. The effect of the geometry of the nanofillers on the dielectric permittivity, polarization, breakdown strength, ECE and crystallinity of the ferroelectric polymer has been systematically investigated. Simulations based on the phase-field model have been carried out to substantiate the experimental results. With the remarkable cooling energy density and refrigerant capacity, the polymer nanocomposites are promising for solid-state cooling applications.

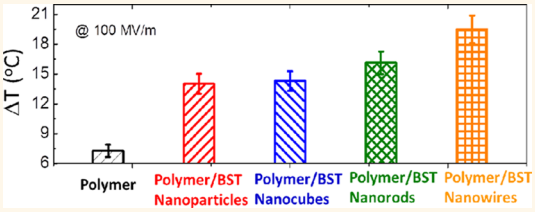

KEYWORDS: electrocaloric effect · polymer nanocomposites · ferroelectrics · nanostructures

Ferroelectric materials possess a spontaneous electrical polarization that can be reversed by the application of an external electric field. Electric-field control of electrical polarization enables a variety of potential applications of ferroelectric materials in advanced devices such as sensors, memories, actuators and capacitors.[1] One peculiar feature associated with the manipulation of polarization of ferroelectric materials by means of an external field is a reversible temperature under adiabatic conditions, a phenomenon known as the electrocaloric effect (ECE).[2−8] The ECE has been regarded as one of the most promising mechanisms for next-generation cooling technologies that can replace conventional gas compression/expansion refrigeration. In addition, it eliminates the use of ozone-depleting or greenhouse gas-emitting refrigerants and simultaneously possesses superior energy efficiency.[2−8] Moreover, the ECE provides an effective route to compact, solid-state devices with high cooling power densities for on-chip thermal management of microelectronic, optoelectronic and biomedical devices.[3,9,10]

Although the ECE has been investigated for many decades, it is only very recently that a significant ECE has been obtained in thin films of ferroelectric ceramics and polymers.[11,12] For example, Mischenko *et al.* reported an adiabatic temperature change (ΔT) of 12 °C and an isothermal

* Address correspondence to wang@matse.psu.edu, jsl@hust.edu.cn.

Received for review March 27, 2015 and accepted June 29, 2015.

Published online July 01, 2015
10.1021/acsnano.5b03371

entropy change (ΔS) of 8 J kg^{-1} K^{-1} in $Pb(Zr_{0.95}Ti_{0.05})O_3$ (PZT) films near the ferroelectric Curie temperature of 222 °C.[11] Ferroelectric poly(vinylidene fluoride-*co*-trifluoroethylene), P(VDF-TrFE), and poly(vinylidene fluoride-*ter*-trifluoroethylene-*ter*-chlorofluoroethylene), P(VDF-TrFE −CFE), have shown a ΔT of 12 °C and a ΔS of 60 J kg^{-1} K^{-1} at 80 and 55 °C, respectively, by Zhang *et al.*[12] While these studies represent major technological breakthroughs, there is still a lack of high-performance EC materials that are easily processed and can be operated at ambient temperature and under a wide range of electric fields for solid-state refrigeration. Although ceramic materials have a high ΔT per unit applied voltage and large thermal conductivity, they are limited by their relatively small breakdown strength and generally require high-temperature sintering in thin-film fabrication.[5,6,13,14] On the other hand, ferroelectric polymers outperform their ceramic counterparts in terms of breakdown strength and processability but suffer from low EC strength; *i.e.*, high electric fields are needed to drive the dipole orientation and induce the ECE in these polymers.[2,12,15]

More recently, remarkable room-temperature ECEs in solution-processable ferroelectric polymer nanocomposites have been demonstrated by integrating the complementary properties of the ferroelectric polymer matrix and ferroelectric ceramic nanofillers.[16,17] However, it is found that the improvement in ECE is generally limited by the content of ceramic nanoparticles because of the sharp decrease in dielectric breakdown strength with the increase of filler content. In this contribution, the effect of nanomorphology of ceramic fillers on the dielectric and EC properties of the polymer nanocomposites has been investigated. Compared to the polymer nanocomposites composed of ferroelectric nanoparticles (NPs), nanocubes (NCs) and nanorods (NRs), the nanocomposites consisting of ferroelectric nanowires (NWs[18−21]) exhibit much higher breakdown and EC strengths as a direct consequence of the high aspect ratio of nanofillers, and consequently, greater ECE. The phase-field simulations confirm the critical role of geometry of ceramic fillers on the enhancement in electrical displacement and reduced inhomogeneity in electric field distribution of the polymer nanocomposites. This work opens up a facile and effective route to development of practically applicable solid-state cooling materials *via* tuning morphology of the ceramic nanostructures in polymer nanocomposites. The greatly improved ECE observed in the polymer nanocomposites not only is one of the largest compared to previously studied EC materials, but also surpasses those of the recently reported giant magnetocaloric effect.[2,22−25]

RESULTS AND DISCUSSION

Materials. It is widely accepted that variations in the external field induce large polarization changes and pronounced ECEs when operating the material in the vicinity of ferroelectric phase transitions.[26] For an ambient-temperature ECE, both Curie temperatures (T_c) of ferroelectric P(VDF-TrFE-CFE) (62.3/29.9/7.8 mol %) terpolymer matrix and $Ba_{0.67}Sr_{0.33}TiO_3$ (BST) nanofiller were adjusted to be ~26 °C by varying their chemical compositions.[16] The ferroelectric terpolymer was synthesized *via* suspension radical polymerization.[27,28] BST NPs with an average diameter of ~180 nm (Figure 1a,b) were prepared by a hydrothermal reaction from TiO_2 NPs, while the hydrothermal conversion of sodium titanate ($Na_2Ti_3O_7$) NWs (Figure S1 in the Supporting Information) using an aqueous solution of $Ba(OH)_2 \cdot 8H_2O$ and $Sr(OH)_2 \cdot 8H_2O$ yielded BST NWs[29,30] with an average length of ~10 μm and mean diameter of ~120 nm (aspect ratio: ~80, Figure 1c,d). The diffusion of Ba^{2+} and Sr^{2+} ions into the precursors is evidenced by the emergence of the elemental signals of Ba and Sr in the energy-dispersive X-ray spectra (EDS, insets of Figure 1a,c). X-ray diffraction (XRD) patterns shown in Figure 1e are suggestive of tetragonal perovskite phase of BST NPs and NWs. The single crystalline structures of these materials were verified from electron diffraction patterns (top right insets of Figure 1b,d). As summarized in Table S2 in the Supporting Information, the lattice constants (*c* and *a*) calculated on the basis of the XRD diffraction patterns[31] (Figures S2, S3 and Table S1 in the Supporting Information) point out that the BST NPs and NWs have a similar lattice constant *a*, but the NWs have a larger *c* which results in a higher *c*/*a* ratio and a larger lattice volume compared to those of NPs. The lattice parameters determined from the XRD patterns are in accordance with the results observed from the interlayer distances between adjacent lattice fringes in the high-resolution transmission electron microscopy (HRTEM) images (bottom left insets of Figure 1b,d), in which the interplanar distances between (100) and (001) denote the *a* and *c* axis, respectively. In addition, BST NCs with an average side length of 200 nm and NRs with an average length of 3 μm, a mean diameter of 300 nm and an aspect ratio of ~10 have been synthesized (Figure S4 in the Supporting Information) *via* the two-step hydrothermal reaction.[29,30]

The nanocomposite thin films were prepared by casting the DMF solution of P(VDF-TrFE-CFE) with BST nanofillers. The cross-sectional scanning electron microscope (SEM) images of the nanocomposites shown in Figure 1f,g and Figure S4b,d in the Supporting Information indicate well-dispersed nanofillers throughout the polymer matrix, which is also manifested in the electric displacement−electric field (*D*−*E*) loops.[32] As shown in Figure S5a−c in the Supporting Information, the remnant displacement, *i.e.*, *D* at zero electric field, arises mainly from the polymer matrix and are almost independent of the filler content.

Dielectric Properties and Polarization. It is informative to examine the dielectric properties and electrical

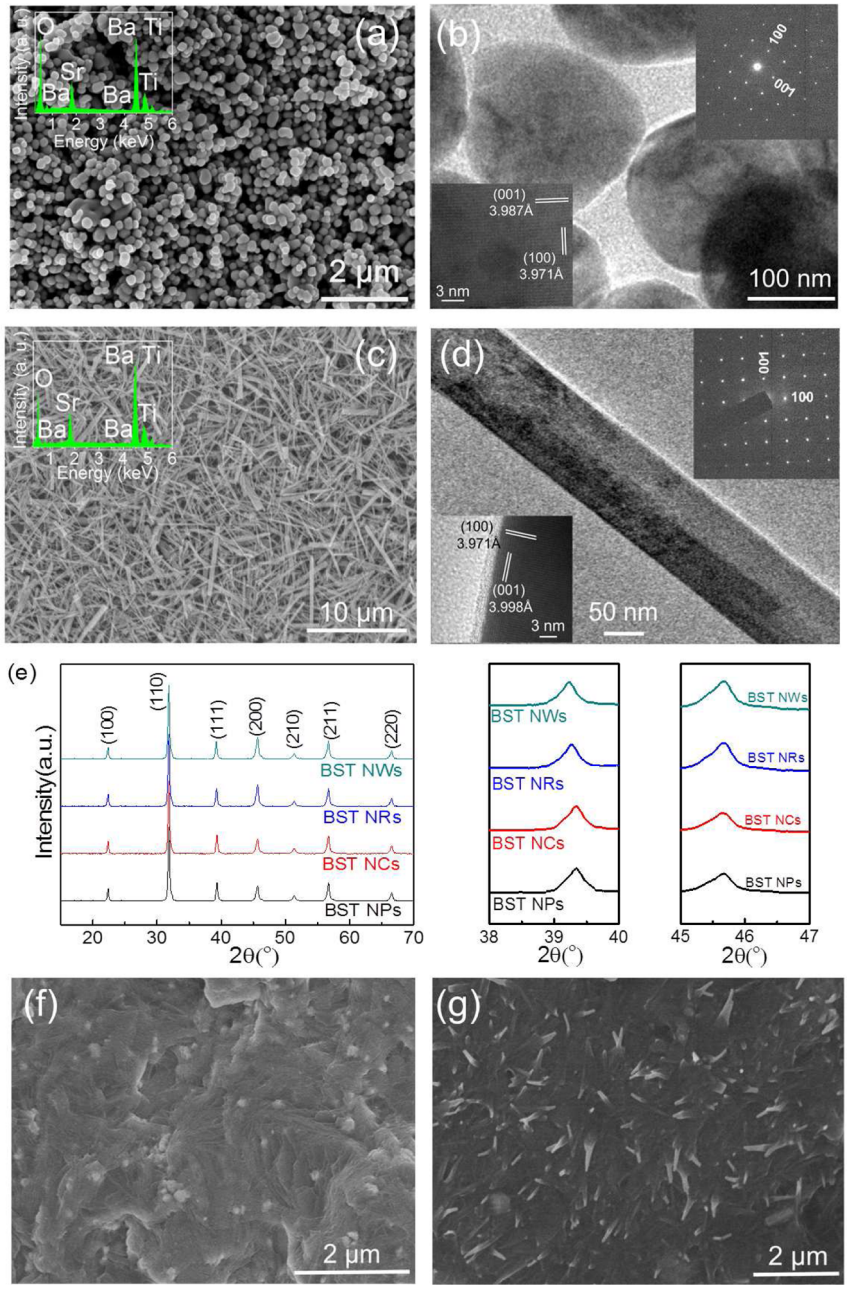

Figure 1. (a) SEM image of the BST NPs. Inset: EDS spectrum of the BST NPs. (b) TEM image of the BST NPs (top right and bottom left insets are the electron diffraction pattern and crystal lattice fringes of the NPs, respectively). (c) SEM image of the BST NWs. Inset: EDS spectrum of the BST NWs. (d) TEM image of the BST NWs (top right and bottom left insets are the electron diffraction pattern and crystal lattice fringes of the NWs, respectively). (e) XRD patterns of the BST NPs, NCs, NRs and NWs. Detailed diffraction profiles around $2\theta = 39°$ and 46° are shown for each sample. (f) Cross-section SEM image of the P(VDF-TrFE-CFE)/10 vol % BST NPs nanocomposite. (g) Cross-section SEM image of the P(VDF-TrFE-CFE)/10 vol % BST NWs nanocomposite.

polarization of the polymer nanocomposites with the BST nanofillers, since the ECE originates from the entropy change as a result of field-induced dipole orientation.[2−7] Clearly, the relative permittivity (ε_r) of the nanocomposites is greatly enhanced upon the incorporation of BST (Figure 2a and Figure S6 in the Supporting Information). Interestingly, the nanocomposites with the BST NWs have a higher ε_r than those of the polymer filled with the same content of the BST NPs, NCs, and NRs, as exhibited in Figure 2a and Figure S6c in the Supporting Information. For instance, ε_r of the nanocomposite containing 15 vol % of the BST NWs reaches 72.5 at 1 kHz, which is 20% higher than that of the polymer nanocomposite with 15 vol % BST NPs.

The profound effect of the BST NWs on the improvement of ε_r of the nanocomposites can be ascribed to the shape effect of the nanoinclusions. As revealed by the XRD and TEM studies, the BST NWs have a larger lattice volume and a higher *c/a* ratio

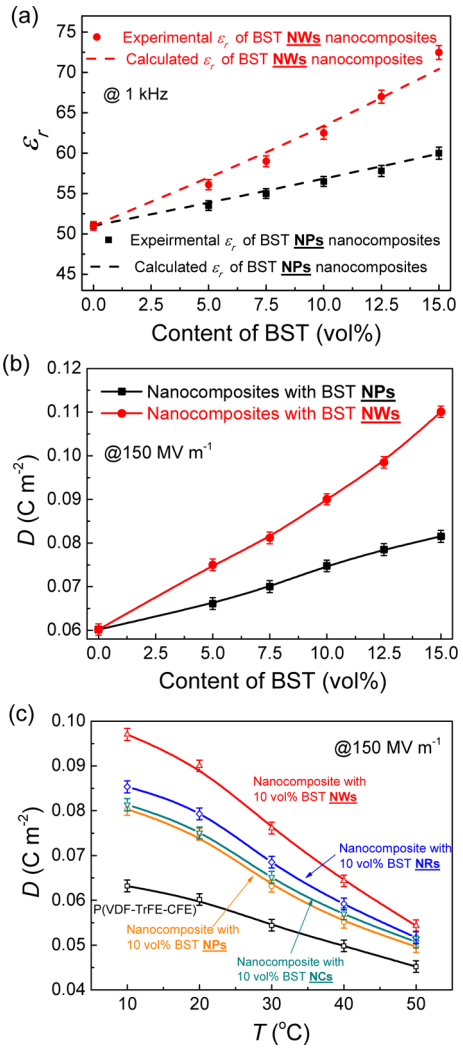

Figure 2. (a) Dependence of relative permittivity (ε_r) of the nanocomposites on the volume fraction of fillers measured at 1 kHz. The dash lines represent ε_r calculated by using the MG and PVS effective medium theories. (b) The electric displacement (*D*) of the nanocomposites as a function of fillers content measured at 150 MV m^{-1}. (c) Temperature dependence of *D* of P(VDF-TrFE-CFE) and the nanocomposites with 10 vol % BST NPs, NCs, NRs and NWs, respectively. Error bars: Standard error.

in lattice constant (Table S2 in the Supporting Information), indicating a larger activity space for B site ions (Ti^{4+}) and a higher relative displacement between B site ions and O^{2-} ions when compared to the NPs. In displacement-type perovskite ferroelectrics, the dipole moment increases with the relative displacement between the B site ions and O^{2-} ions.[33,34] Therefore, the BST NWs with a higher ε_r lead to a larger permittivity of the polymer nanocomposites relative to the corresponding BST NP, NC and NR based nanocomposites. The effective permittivities of the polymer nanocomposites with the BST NPs and NWs are computed using the Maxwell–Garnett (MG) effective medium theory (eq 1) and the Polder–Van Santen (PVS) formalism (eq 2),[35] which are typically used to analyze the dielectric permittivity of nanocomposites with spheroidal and linear inclusions, respectively, where ε_a and f_a are the relative permittivity and volume fraction of the fillers, respectively, and ε_b is the relative permittivity of the matrix. It can be seen from Figure 2a that the calculated ε_r of the nanocomposites with the BST nanofillers agree fairly well with the measured values. As shown in Figure S6c in the Supporting Information, the nanocomposites with 10 vol % BST NPs and NCs have similar ε_r values which are slightly lower than that of 10 vol % BST NR-containing nanocomposite but significantly smaller when compared to that of the polymer nanocomposite with 10 vol % BST NWs; this further indicates that the ε_r of the nanocomposites are strongly dependent on the aspect ratio of the nanofillers.

$$\varepsilon_{\text{eff}} = \varepsilon_b \left[\frac{\varepsilon_a + 2\varepsilon_b + 2f_a(\varepsilon_a - \varepsilon_b)}{\varepsilon_a + 2\varepsilon_b - f_a(\varepsilon_a - \varepsilon_b)} \right] \quad (1)$$

$$\varepsilon_{\text{eff}} = \varepsilon_b + \frac{f_a}{3}(\varepsilon_a - \varepsilon_b) \sum_{j=x,y,z} \left[\frac{\varepsilon_{\text{eff}}}{\varepsilon_{\text{eff}} + N_j(\varepsilon_a - \varepsilon_{\text{eff}})} \right] \quad (2)$$

Figure S5 in the Supporting Information presents the *D*–*E* loops of the nanocomposites with various contents of the BST nanofillers measured at 150 MV m^{-1}. Figure 2b summarizes the *D* of the polymer nanocomposites as a function of filler content. Consistent with weak-field dielectric spectra, *D* of the polymer nanocomposites increases steadily from 0.06 C m^{-2} for P(VDF-TrFE-CFE) to 0.08 C m^{-2} as the BST NPs concentration increases to 15 vol %, due to the higher polarization of the nanoinclusions. Again, the BST NWs based nanocomposites exhibit higher *D* values than those of the BST NP-containing polymer nanocomposites, *e.g.*, 0.11 *vs* 0.08 C m^{-2} at 15 vol % filler content. Furthermore, as shown in Figure S5d in the Supporting Information, the BST NWs based nanocomposites exhibit the highest *D* values than those of the BST NP, NC and NR-containing polymer nanocomposites, *e.g.*, 0.09 *vs* 0.075 (NP and NC), and 0.08 (NR) C m^{-2} at 10 vol % filler content, indicating that *D* of the nanocomposites increase steadily with the aspect ratio of the ferroelectric nanoinclusions, which are in line with the simulation results calculated by using the phase-field model (see Methods for the details).[36,37] The lower *D* values in the BST NP and NC nanocomposites could be ascribed to the high depolarization field on the nanofillers caused by the low permittivity of the polymer matrix.[38,39] Since the depolarization field in the nanofillers can be significantly depressed by increasing their length,[40] the polymer nanocomposites whose nanofillers possess higher aspect ratio (such as NWs) exhibit much larger *D* than the other nanocomposites.

According to the Maxwell relations which describes the relationship between *D* and temperature *T*,[11,12]

$$\Delta S = -\int_{E1}^{E2} (\partial D/\partial T)_E \, dE \quad (3)$$

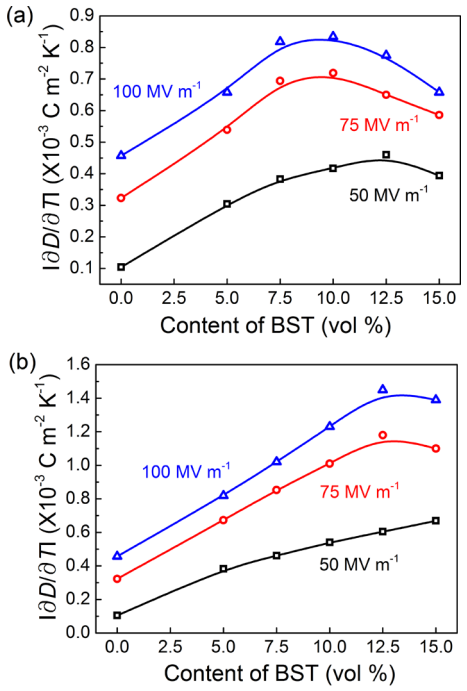

Figure 3. Filler content dependence of $|\partial D/\partial T|$ of P(VDF-TrFE-CFE) with the BST (a) NPs and (b) NWs, respectively.

$$\Delta T = -\frac{1}{\rho}\int_{E1}^{E2}\frac{T}{C_p}(\partial D/\partial T)_E \, dE \qquad (4)$$

where ρ is density and C_p is the specific heat, it is accepted that the appearance of a larger $|\partial D/\partial T|$ tends to bring about greater ECE. As a typical pyroelectric material,[41,42] BST shows sharply decreased D with increasing temperature around T_c, resulting in a large slope of $D-T$ curve and a high $|\partial D/\partial T|$.[16] Consequently, the incorporation of BST into the polymer leads to steeper $D-T$ curves and larger $|\partial D/\partial T|$ values of the nanocomposites when compared to the neat polymer, as shown in Figure 2c and Figure 3. The NW based polymer nanocomposites are found to display the steepest $D-T$ curves in comparison to the NP, NC and NR-containing nanocomposites, which accounts for the superior ECE observed in the polymer nanocomposites, especially with the NW fillers (see the sections below).

Effect of Nanofillers on Dielectric Strength. Dielectric strength (E_b) is the maximum electric field that can be applied across the materials without causing breakdown, and consequently, determines the magnitude of ECE that can be achieved in the samples. It is noteworthy that the geometry of nanofillers also affects the dielectric strength of the polymer nanocomposites. Figure S7 in the Supporting Information presents E_b of the polymer nanocomposites analyzed by using a two-parameter Weibull cumulative probability function.[43] It is found that the polymer nanocomposites with the BST NWs have the greatest E_b than the respective nanocomposites with the BST NPs, NCs and NRs, *e.g.*, at 10 vol % loading of the nanofillers, 303 MV m^{-1} of the BST NW based nanocomposite *vs* 277, 267, and 282 MV m^{-1} of the nanocomposite with the BST NPs, NCs and NRs, respectively. At ambient temperature, polymer materials are known to mainly fail through the avalanche and electromechanical breakdown.[44,45] As depicted in Figure S8 in the Supporting Information, the electrical resistivity of the nanocomposites decreases with the content of BST and is essentially independent of filler shape before reaching the percolation threshold. This finding apparently excludes the contributions of electrical conductivity to the difference in E_b of the BST NP, NC, NR and NW based polymer nanocomposites. By contrast, it is evident from Figure S9 in the Supporting Information that the Young's modulus of polymer nanocomposites is strongly associated with geometry of nanofillers, and again, the BST NWs nanocomposites exhibit the largest Young's modulus than the polymers filled with NPs, NCs and NRs. For instance, Young's modulus of the nanocomposite with 15 vol % BST NWs is 490 MPa, which is ~30% higher than that of the polymer nanocomposite with the same content of the BST NPs. The effect of filler shape on the mechanical strength of nanocomposites can be quantitatively explained by using the empirical models, such as the Halpin–Tsai equation, which suggests the Young's modulus of the nanocomposites increases with the respect ratio of fillers.[46] According to the electromechanical mechanism, the critical electric field of mechanical collapse in dielectric materials, which can be approximated by eq 5 (where Y is the Young's modulus and ε_0 is the vacuum permittivity), increases with square root of the Young's modulus.[45] Thus, the higher moduli of the BST NW nanocomposites lead to larger electromechanical $E_{b(\mathrm{mech})}$ than the corresponding NP, NC and NR containing polymer nanocomposites (Figure S9 in the Supporting Information).

$$E_{b(\mathrm{mech})} = 0.606\left[\frac{Y}{\varepsilon_0\varepsilon_r}\right]^{1/2} \qquad (5)$$

In particular, the breakdown process is accelerated by the presence of highly inhomogeneous electric fields in polymer nanocomposites arising because of a large contrast in permittivity between polymer and filler phases.[47] We employ the phase-field model[36,37] to simulate the electric field distribution in the polymer nanocomposites with the BST NPs, NCs, NRs and NWs (Figure 4). With an applied vertical electric field of 320 MV m^{-1}, a strong polarization response is induced in the nanofillers, which raises the local electric field in vertical adjacent regions (Figure 4b,d,f,h). The electric field is especially concentrated in regions between two (or more) nanofillers which are close to each other, where local breakdown would be most likely triggered. Compared with the BST NP and NC nanocomposites where regions with high electric field extend from the

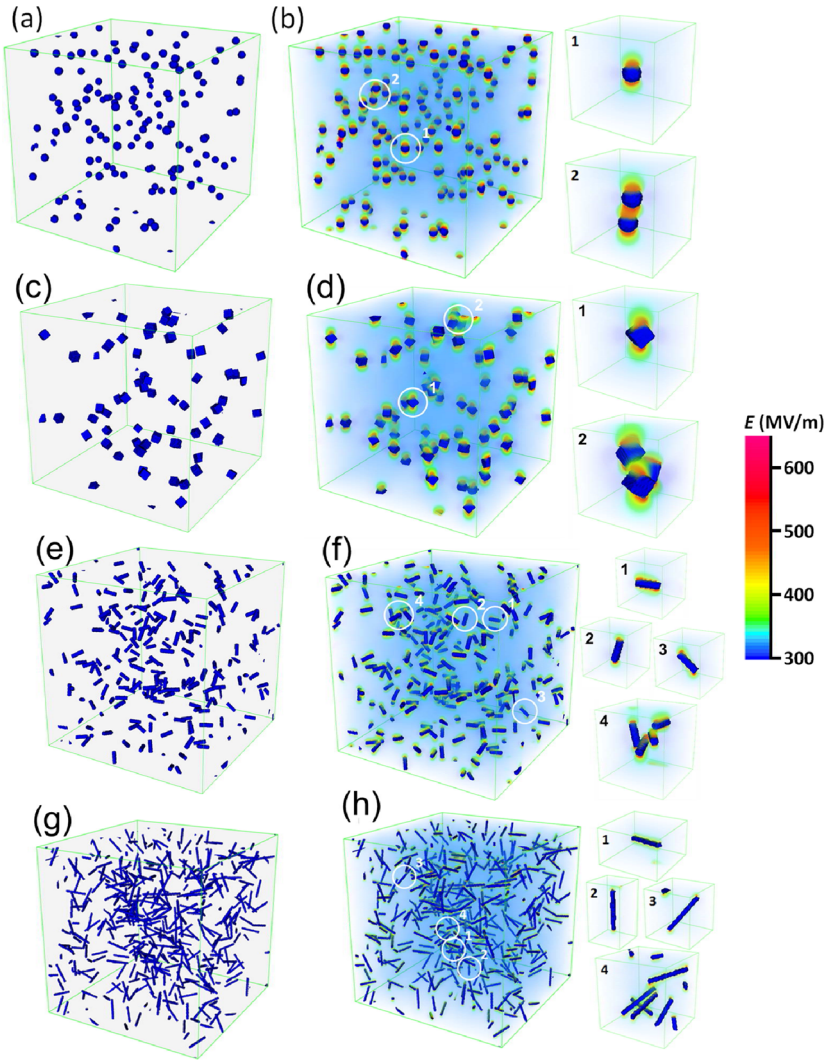

Figure 4. Electric field distribution in P(VDF-TrFE-CFE)/BST nanocomposites modeled using a phase-field approach. (a,c,e,g) Initial two-phase distribution of the P(VDF-TrFE-CFE) nanocomposites with 7.5 vol % BST NPs, NCs, NRs and NWs. The blue spheres, cubes, rods and wires represent the BST NPs, NCs, NRs and NWs, respectively. (b,d,f,h) Corresponding electric field distribution in the P(VDF-TrFE-CFE) matrix on applying a vertical electric field. The right panels are enlarged views of the circled regions containing single or multiple nanofillers.

phase interface far into the P(VDF-TrFE-CFE) matrix, around the BST NRs and NWs with various orientations, electric fields in the P(VDF-TrFE-CFE) matrix are only elevated in relatively smaller regions vertically adjacent to the phase interface, due to the higher aspect ratio of the NRs and especially, the NWs. Electric fields in regions among multiple NRs and NWs are less strong compared with regions among multiple NPs and NCs, and therefore less likely to induce a local breakdown. This difference in electric field distribution, coupled with Young's modulus, is believed to play an important role in determining E_b of the P(VDF-TrFE-CFE)/BST nanocomposites.

Dependence of ECE on Morphology of Nanofillers. The ECE was investigated by direct measurements of the isothermal heat (Q) of the films using a high-resolution heat flux sensor during the cooling cycles.[16,48] Q is defined as the cooling energy density, with the accompanying ΔS and ΔT deduced from $Q = T\Delta S = \int_T^{T+\Delta T} C_p \, dT$.[2] It should be noted that, although ΔS and ΔT are typical parameters to evaluate the ECE, the value of Q is of prime importance for cooling because only by removal of heat is cooling achieved.[2,49] Figure 5 compares the EC performance of the P(VDF-TrFE-CFE)/BST NP and NW polymer nanocomposites, characterized at room temperature under electric fields ranging from 50 to 100 MV m^{-1}. The first evident result is the confirmation of the presence of a much larger ECE in the polymer nanocomposites when compared to their constituents. For example, Q, ΔT and ΔS values of the polymer nanocomposite with a 12.5 vol % BST NPs are about 3-fold greater than those of the pristine P(VDF-TrFE-CFE) at an electric field of 50 MV m^{-1}. More impressively, much greater enhancements in ECE have been achieved in the BST NW based polymer nanocomposites; for example, Q, ΔT and ΔS of the

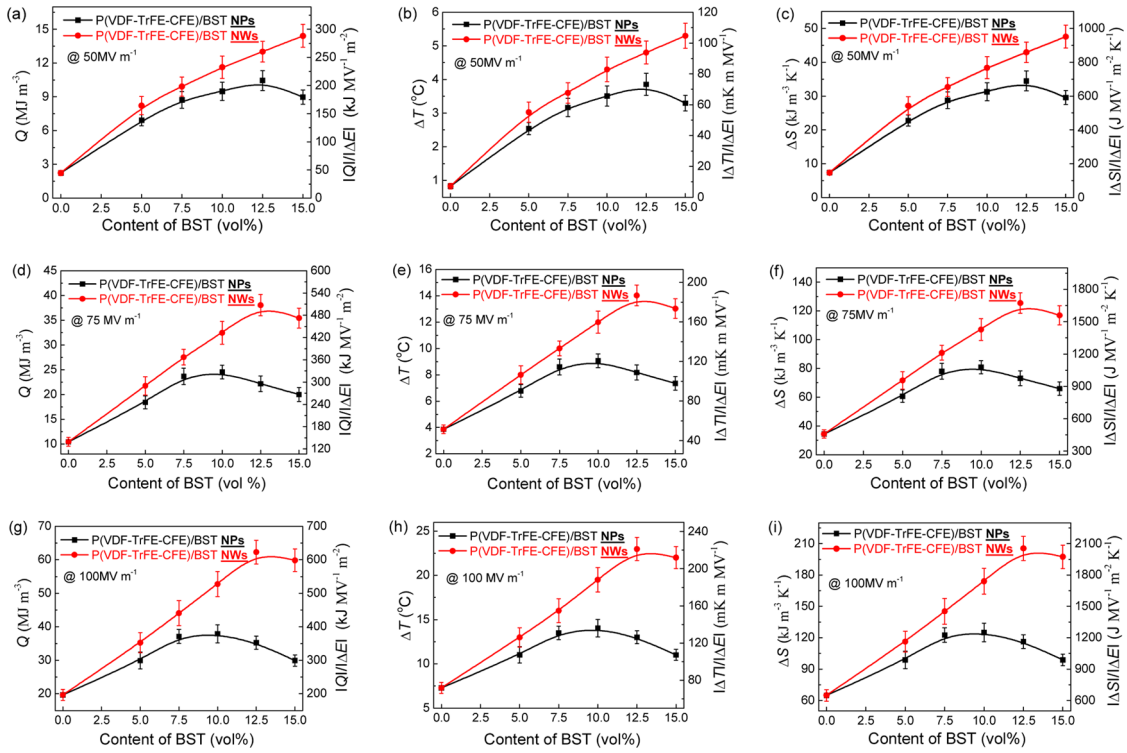

Figure 5. (a) Q and $|Q|/|\Delta E|$, (b) ΔT and $|\Delta T|/|\Delta E|$, (c) ΔS and $|\Delta S|/|\Delta E|$ at 50 MV m^{-1}; (d) Q and $|Q|/|\Delta E|$, (e) ΔT and $|\Delta T|/|\Delta E|$, (f) ΔS and $|\Delta S|/|\Delta E|$ at 75 MV m^{-1}; (g) Q and $|Q|/|\Delta E|$, (h) ΔT and $|\Delta T|/|\Delta E|$, (i) ΔS and $|\Delta S|/|\Delta E|$ at 100 MV m^{-1}. Error bars: Standard error.

nanocomposite with 15 vol % loading of BST NWs reached 14.4 MJ m^{-3}, 5.3 °C, and 47.5 kJ m^{-3} K^{-1}, respectively, all of which are ~6.5 times those of P(VDF-TrFE-CFE) at 50 MV m^{-1}. Coinciding with notable improvements in Q, ΔT and ΔS, the EC strengths represented by the values of $|Q|/|\Delta E|$, $|\Delta S|/|\Delta E|$ and $|\Delta T|/|\Delta E|$ increase significantly with the incorporation of BST into the polymer matrix. For instance, the nanocomposite with 12.5 vol % BST NWs has a $|\Delta S|/|\Delta E|$ of 2.0 kJ MV^{-1} m^{-2} K^{-1} at 100 MV m^{-1}, which is more than 3 times higher than that of P(VDF-TrFE-CFE) and already exceeds those of PZT and PMN−PT thin films (*i.e.*, ~1.3 kJ MV^{-1} m^{-2} K^{-1}).[11,12,50] For a 1-μm thin film, a ΔT of 22.5 °C can be obtained in the polymer nanocomposites at a voltage of 100 V, indicating that substantial ECE can be generated even by using residential wiring voltages. For comparison, 150 V must be applied to the neat polymer to realize a ΔT of 16 °C. An electric field of 72.3 MV m^{-1} is required to generate a ΔT of 9 °C in PMN−PT films at room temperature.[50] These results demonstrate that the polymer nanocomposites can be efficiently operated under modest electric fields, which overcomes the key limitation of EC polymers mentioned above.

It is worthy of note that the polymer nanocomposites exhibit different dependences of the ECE on the contents of NWs and NPs, as shown in Figure 5. For example, at 50 MV m^{-1}, the ECE is maximized at 12.5 vol % NPs and 15 vol % NWs, respectively, while at electric fields of 75 and 100 MV m^{-1}, the optimized contents of nanofillers are 10 vol % for NPs and 12.5 vol % for NWs. It is found that these results match closely the trends shown in $|\partial D/\partial T|$ *vs* filler content and applied fields (Figure 3), suggesting that the Maxwell relations, which are thermodynamic models providing a convenient link between D and changes of S, are nevertheless a reasonable theoretical description of the ECE even though the current understanding of the ECE in relaxor ferroelectrics such as P(VDF-TrFE-CFE) terpolymer and its nanocomposites remains elusive.[2−6]

Furthermore, as summarized in Figure 6, it is found that the polymer nanocomposites containing 10 vol % BST NPs and NCs exhibit similar ECE which are lower than that of BST NR and NW based polymer nanocomposites. For example, at 100 MV m^{-1}, the nanocomposites with 10 vol % BST NPs and NCs shows a ΔT of ~14 °C, while the nanocomposites with the same content of the BST NRs and NWs have a ΔT of ~17 °C and ~20 °C, respectively. These results suggest the ECE of the nanocomposites is also closely related to the aspect ratio of the ceramic nanofillers, which is in accordance with the trends shown in polarization and dielectric properties of the polymer nanocomposites.

The polymer nanocomposites permit the application of high electric fields to achieve giant ECE. Even though the breakdown strength degrades with the increase of the filler content, which is often observed in dielectric polymer nanocomposites,[51] the BST containing polymer nanocomposites maintain relatively high Weibull characteristic breakdown strengths, *e.g.*, well

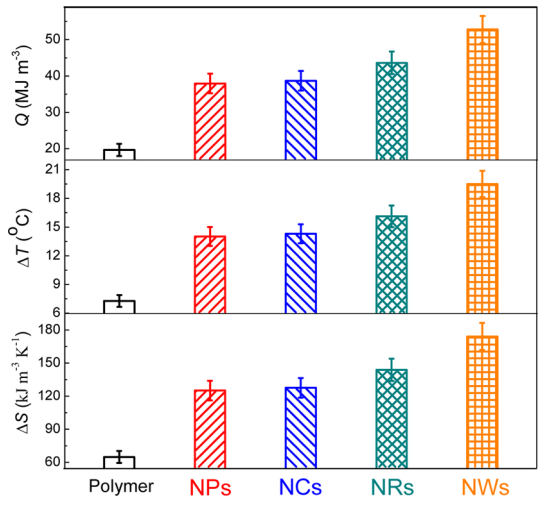

Figure 6. Q, ΔT and ΔS of the P(VDF-TrFE-CFE) and its nanocomposites with 10 vol % BST NPs, NCs, NRs and NWs measured at 100 MV m^{-1}. Error bars: Standard error.

above 200 MV m^{-1} even at 15 vol % nanofiller content (Figure S7 in the Supporting Information). By contrast, the electric fields applied on the EC ceramic thin films and bulk materials are typically below 100 and 10 MV m^{-1}, respectively,[52,53] which critically limits the magnitude of the obtained ECE. The best ECE found in BST is Q of 7.97 MJ m^{-3}, ΔT of 3.1 °C and ΔS of 27.3 kJ m^{-3} K^{-1}.[54] As shown in Figure 7 and Figure S10 in the Supporting Information, with the application of an electric field of 150 MV m^{-1}, a colossal ECE is attained with a Q of 84.2 MJ m^{-3}, ΔT of 32 °C, and ΔS of 272.8 kJ m^{-3} K^{-1} in the polymer nanocomposites with 10 vol % BST NWs. In addition to the high Q, the refrigerant capacity, a parameter used to assess the refrigerant performance, of the polymer nanocomposite of $\Delta T\Delta S$ = 8.73 MJ m^{-3} is one of the highest values reported so far in EC ceramics and polymers.[2]

As a direct consequence of its lower E_b, high electric fields can only be applied on the BST NP containing polymer nanocomposites with a less filler content, leading to inferior ECE than the respective NW based nanocomposites. For example, the polymer nanocomposite containing 7.5 vol % BST NPs has a similar E_b, *i.e.*, ~300 MV m^{-1}, with the nanocomposite with 10 vol % BST NWs (Figure S7 in the Supporting Information). An applied field of 150 MV m^{-1} yields a Q of 63.4 MJ m^{-3}, a ΔT of 23 °C, and a ΔS of 209.2 kJ m^{-3} K^{-1} of the polymer nanocomposites with 7.5 vol % BST NPs, which are significantly lower than those of the nanocomposites with 10 vol % BST NWs (Figure 7 and Figure S10 in the Supporting Information). Note that in our ECE measurements, the maximum applied field is purposely set at about half of E_b, as dictated by the theoretical calculations of the devices intended to have a lifetime greater than 10 years.[55]

Effect of Nanofillers on Polymer Crystallinity. Furthermore, we note that the BST NWs and NPs affect the

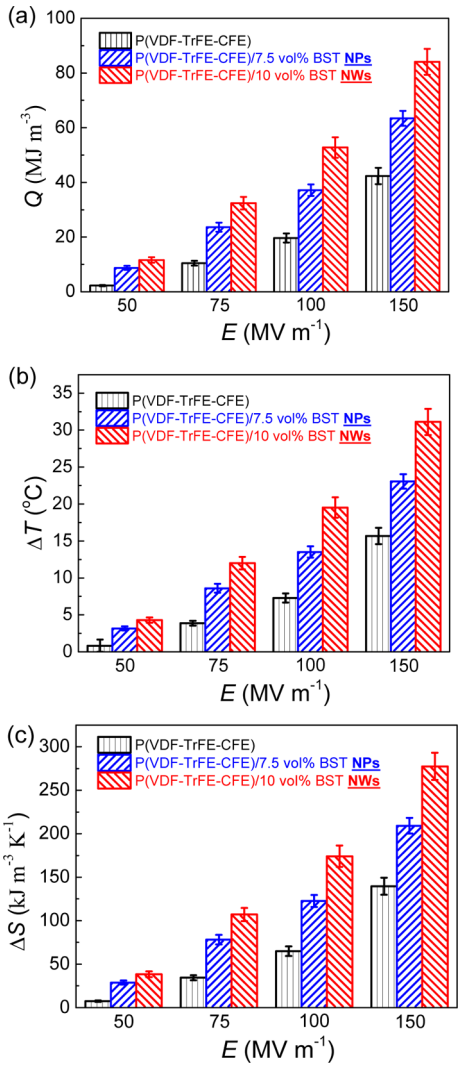

Figure 7. (a) Q, (b) ΔT and (c) ΔS of P(VDF-TrFE-CFE) and the nanocomposites with 7.5 vol % NPs and 10 vol % NWs under different electric fields. Error bars: Standard error.

crystallization behavior of the polymer matrix to different degrees. Although both the NWs and NPs improve the crystallinity of the polymer, as shown in differential scanning calorimetry (DSC) measurements (Figure S11 in the Supporting Information), the NWs give rise to a slightly larger degree of crystallinity of the polymer than the NPs at the same filler content. For instance, the degree of crystallinity increases from 38.1% of polymer to 43.0% with the introduction of 10 vol % NWs, whereas the corresponding crystallinity is 41.5% at 10 vol % NPs. In the meantime, the presence of the NWs and NPs in the polymer matrix monotonically decreases the crystallite size of the polymer, which is corroborated by the XRD studies (Figure S12 in the Supporting Information). Interestingly, at the same filler content, the NWs lead to a smaller crystallite size of the polymer in comparison to the NPs, *e.g.*, 42 nm *vs* 47 nm at 10 vol % NWs and NPs, respectively. It is known that a larger crystallinity yields higher polarization and a crystallite with a smaller size shall

be easier to be oriented under the applied field.[56] It is thus postulated that the differences in crystallinity and crystallite size caused by the NWs and NPs may likewise contribute to their different amplitudes of ECE and EC strength observed in the polymer nanocomposites.

CONCLUSIONS

Markedly enhanced ECE has been observed in the polymer nanocomposites consisting of a ferroelectric polymer matrix and BST nanofillers at room temperature, which is attributable to improved polarization and larger changes of polarization with temperature arising from the introduced BST nanofillers and the high breakdown strength of the polymer matrix. By capitalizing on the synergy of the ceramic nanofillers and the polymer matrix, the polymer nanocomposites can effectively operate at both modest and high electric fields to realize pronounced ECEs. More importantly, it is found that the ECE depends intimately on the morphology of the nanofillers, which provides an additional route to enhanced ECE. The preparation of the EC polymer nanocomposites *via* solution casting is straightforward and cost-effective, and can be readily scaled up; this, coupled with technologically viable EC values, makes this class of solid-state refrigerants particularly attractive for practical device applications. Furthermore, it is anticipated that the ECE of these polymer nanocomposites can be further improved by systematically tuning the compositions and morphologies of ferroelectric ceramic nanofillers.

METHODS

Synthesis of BST NPs, NCs, NRs and NWs. BST NPs were prepared using a one-step hydrothermal reaction. $BaCl_2 \cdot 2H_2O$ (Sigma-Aldrich, ACS, 99%) and $SrCl_2 \cdot 6H_2O$ (Sigma-Aldrich, ACS, 99%) were added to 1.2 M NaOH (Sigma-Aldrich, reagent-grade, 98%) aqueous solution. The molar ratio of Ba/Sr was kept at 67/33. The solution was stirred at 80 °C for 2 h. Then the solution was filtered and mixed with TiO_2 (0.25 M, Sigma-Aldrich, ACS, 99%) in an autoclave (PARR 4748A, 200 mL). The autoclave was heated at 200 °C for 20 h. The precipitate was collected, washed with 0.1 M HCl (Sigma-Aldrich, ACS, 37%) aqueous solution, water and ethanol, and then dried at 80 °C for 24 h. BST NCs, NRs and NWs were obtained by a two-step hydrothermal reaction.[29,30] First, sodium titanate NWs were synthesized by hydrothermal reaction. A solution of 10 M sodium hydroxide was mixed with TiO_2 (0.25 M) and placed in the autoclave. The autoclave was heated at 200 °C for 24 h. After the autoclave was cooled to room temperature, the obtained sodium titanate NWs were sequentially washed with 0.2 M hydrochloric acid (Fisher, 37%) and water several times, and dried at 60 °C for 12 h. The sodium titanate NWs were then converted to $Ba_{0.67}Sr_{0.33}TiO_3$ NCs, NRs and NWs by a second hydrothermal reaction in a temperature range of 70 to 200 °C with an aqueous solution containing $Ba(OH)_2 \cdot 8H_2O$ (Aldrich, 98%) and $Sr(OH)_2 \cdot 8H_2O$ (Aldrich, 95%). The concentrations of $Ba(OH)_2 \cdot 8H_2O$+ $Sr(OH)_2 \cdot 8H_2O$ for the preparation of BST NCs, NRs and NWs are 0.1, 0.15, and 0.2 M, respectively. After that, the BST obtained powders were collected and washed, and then dried at 80 °C for 12 h.

Polymer Nanocomposites. P(VDF-TrFE-CFE) was dissolved in DMF at a concentration of 50 mg/mL. BST nano powders were added into the P(VDF-TrFE-CFE) solution with the required ratio under tip-type sonication. The mixture was further sonicated for another 30 min and then cast onto glass plates and dried at 90 °C for 16 h in a vacuum oven. The films were peeled off from the glass plates and annealed at 105 °C for 12 h.

Characterization. XRD was performed using a PANalytical Xpert pro MPD. The radiation source was Cu Kα with a wavelength of 1.54 Å. The morphology of BST was observed using a JEOL JEM-2010F transmission electron microscopy (TEM). A Hitachi S-4800 field emission scanning electron microscope (FE-SEM) was also used to investigate the morphology of the BST and nanocomposite films. DSC curves were acquired using a TA Instruments model Q100 at a heating rate of 10 °C min^{-1}. The specific heat of the samples was also tested by a TA Q100 in modulated mode. The Young's modulus was measured using an Instron 5866 with a 200 N load cell and an extension rate of 20 mm min^{-1}. Gold electrodes of a typical thickness of 60 nm and diameter of 5 mm were sputtered (Denton Vacuum, Desk IV) on both sides of the polymer films for the electrical and ECE measurements. Dielectric spectra were acquired over a broad temperature range using a Hewlett-Packard 4284A LCR meter in conjunction with a Delta Design oven model 2300. Electrical resistivity was obtained under an electric field of 30 MV m^{-1} provided by a Hewlett-Packard 4140B pA meter/voltage source and KEPCO BOP 1000 M amplifier. High-field $D-E$ loops were collected using a modified Sawyer–Tower circuit, where the samples were subjected to a triangular unipolar wave. At least 20 samples were measured for each test. Dielectric breakdown strength measurements were performed on a TREK P0621P instrument using the electrostatic pull-down method under a voltage ramp of 500 V s^{-1}. The breakdown results were analyzed using a two-parameter Weibull distribution function, $P(E) = 1 - \exp(-(E_b/\alpha)^{\beta})$, where $P(E)$ is the cumulative probability of electric failure, E_b is the measured breakdown field, is the characteristic breakdown strength which corresponds to a ~63.2% probability of failure, and β is the slope parameter that evaluates the scatter of data.[43] The details of ECE measurement is presented in previous work.[16,48]

Simulation of Electric Displacement and Field Distribution. The electric displacement and electric field distribution in a composite responsive to an applied electric field was simulated by utilizing a phase-field model.[36,37] Two sets of position-dependent order parameters were used in the model: a nonevolving $\varphi(r)$ for the initial two-phase structure, with $\varphi = 1$ for the BST phase and $\varphi = 0$ for the P(VDF-TrFE-CFE) phase, respectively, where r is the position vector, and the ferroelectric polarization $P_f(r,t)$ describes the ferroelectric domain structure in BST.

The evolution of electric polarization responsive to an external electric field was simulated by solving the time-dependent Ginzburg–Landau equation,[37]

$$\frac{\partial P_f}{\partial t} = -L_P \frac{\delta F}{\delta P_f} \tag{6}$$

where L_P is a kinetic coefficient related to ferroelectric domain evolution. F is the free energy of the composite, expressed following the ferroelectric and dielectric properties of the BST and P(VDF-TrFE-CFE) phases, respectively,[57,58]

$$F(P_f, E) = \int \left[\varphi(f_{\text{Landau}}(P_f) + \mathbf{g}_P(\nabla P_f)^2) + (1-\varphi)\left(\frac{1}{2\varepsilon_0}(\varepsilon)^{-1}P^2\right) - P \cdot E \right] dV \tag{7}$$

where f_{Landau} is the landau energy density, with the Landau coefficients a chosen as a linear combination of those of $BaTiO_3$ and $SrTiO_3$,[59−61] *i.e.*,

$$a = qa_{\text{BTO}} + (1-q)a_{\text{STO}} \tag{8}$$

with q = 0.874 herein corresponding to a Curie–Weiss temperature T_{C-W} = 27.5 °C as experimentally measured; $\mathbf{g}_P$ is a

gradient energy coefficient related to the ferroelectric domain wall energy; ε is a position-dependent relative dielectric permittivity, calculated as

$$\varepsilon = \varphi\varepsilon_{BST} + (1 - \varphi)\varepsilon_{poly} \quad (9)$$

where ε_{BST} and ε_{poly} are the background dielectric permittivity of the BST and the P(VDF-TrFE-CFE) phase, respectively. P is the total electric polarization expressed as

$$P = \varphi P_f + \varepsilon_0 \varepsilon E \quad (10)$$

where the electric field E was further obtained by solving the electrostatic Poisson equation $\nabla \cdot (\varepsilon_0 E + P) = 0$ using a Fourier spectral iterative perturbation method.[62]

Conflict of Interest: The authors declare no competing financial interest.

Acknowledgment. The work was supported by the National Science Foundation (CMMI 1361713, DMR1410714), National Natural Science Foundation of China (51373132, 61378076) and National Key Scientific Instrument and Equipment Development Projects of China (2013YQ160551). G.Z. and X.Z. acknowledge the fellowship provided by the China Scholarship Council (CSC).

Supporting Information Available: Microstructures of the sodium titanate NW templates, BST NCs and NRs, and their nanocomposites; detailed diffraction profiles of the XRD patterns and lattice parameters of the BST nanofillers; dielectric, ferroelectric and mechanical properties, breakdown strength, crystallinity and ECE of the P(VDF-TrFE-CFE)/BST nanocomposites. The Supporting Information is available free of charge on the ACS Publications website at DOI: 10.1021/acsnano.5b03371.

REFERENCES AND NOTES

1. Scott, J. F. Applications of Modern Ferroelectrics. *Science* **2007**, *315*, 954–959.
2. Moya, X.; Kar-Narayan, S.; Mathur, N. D. Caloric Materials Near Ferroic Phase Transitions. *Nat. Mater.* **2014**, *13*, 439–450.
3. Correia,T.; Zhang, Q. *Electrocaloric Materials: New Generation of Cooler*; Springer-Verlag: Berlin, 2014.
4. Alpay, S. P.; Mantese, J.; Trolier-McKinstry, S.; Zhang, Q. M.; Whatmore, R. W. Next-Generation Electrocaloric and Pyroelectric Materials for Solid-State Electrothermal Energy Interconversion. *MRS Bull.* **2014**, *39*, 1099–1108.
5. Valant, M. Electrocaloric Materials for Future Solid-State Refrigeration Technologies. *Prog. Mater. Sci.* **2012**, *57*, 980–1009.
6. Scott, J. F. Electrocaloric Materials. *Annu. Rev. Mater. Res.* **2011**, *41*, 229–240.
7. Lu, S. G.; Zhang, Q. M. Electrocaloric Materials for Solid-State Refrigeration. *Adv. Mater.* **2009**, *21*, 1983–1987.
8. Defay, E.; Crossley, S.; Kar-Narayan, S.; Moya, X.; Mathur, N. D. The Electrocaloric Efficiency of Ceramic and Polymer Films. *Adv. Mater.* **2013**, *25*, 3337–3342.
9. Jia, Y.; Sungtaek Ju, Y. A Solid-State Refrigerator Based on the Electrocaloric Effect. *Appl. Phys. Lett.* **2012**, *100*, 242901.
10. Plaznik, U.; Kitanovski, A.; Rozic, B.; Malic, B.; Ursic, H.; Drnovsek, S.; Cilensek, J.; Vrabelj, M.; Poredos, A. Bulk Relaxor Ferroelectric Ceramics as a Working Body for an Electrocaloric Cooling Device. *Appl. Phys. Lett.* **2015**, *106*, 043903.
11. Mischenko, A. S.; Zhang, Q.; Scott, J. F.; Whatmore, R. W.; Mathur, N. D. Giant Electrocaloric Effect in Thin-Film $PbZr_{0.95}Ti_{0.05}O_3$. *Science* **2006**, *311*, 1270–1271.
12. Neese, B.; Chu, B. J.; Lu, S. G.; Wang, Y.; Furman, E.; Zhang, Q. M. Large Electrocaloric Effect in Ferroelectric Polymers Near Room Temperature. *Science* **2008**, *321*, 821–823.
13. Peng, B.; Fan, H.; Zhang, Q. A Giant Electrocaloric Effect in Nanoscale Antiferroelectric and Ferroelectric Phases Coexisting in a Relaxor $Pb_{0.8}Ba_{0.2}ZrO_3$ Thin Film at Room Temperature. *Adv. Funct. Mater.* **2013**, *23*, 2987–2992.
14. Zhao, Y.; Hao, X.; Zhang, Q. Energy-Storage Properties and Electrocaloric Effect of $Pb_{(1-3x/2)}La_xZr_{0.85}Ti_{0.15}O_3$ Antiferroelectric Thick Films. *ACS Appl. Mater. Interfaces* **2014**, *6*, 11633–11639.
15. Moya, X.; Stern-Taulats, E.; Crossley, S.; Alonso, D. G.; Narayan, S. K.; Planes, A.; Mañosa, L.; Mathur, N. D. Giant Electrocaloric Strength in Single-Crystal $BaTiO_3$. *Adv. Mater.* **2013**, *25*, 1360–1365.
16. Zhang, G.; Li, Q.; Gu, H.; Jiang, S.; Han, K.; Gadinski, M. R.; Haque, M. A.; Zhang, Q. M.; Wang, Q. Ferroelectric Polymer Nanocomposites for Room-Temperature Electrocaloric Refrigeration. *Adv. Mater.* **2015**, *27*, 1450–1454.
17. Li, Q.; Zhang, G.; Zhang, X.; Jiang, S.; Zeng, Y.; Wang, Q. Relaxor Ferroelectric-Based Electrocaloric Polymer Nanocomposites with a Broad Operating Temperature Range and High Cooling Energy. *Adv. Mater.* **2015**, *27*, 2236–2241.
18. Morrison, F. D.; Luo, Y.; Szafraniak, I.; Nagarajan, V.; Wehrspohn, R. B.; Steinhart, M.; Wendroff, J. H.; Zakharov, N. D.; Mishina, E. D.; K. Vorotilov, A.; *et al.* Ferroelectric Nanotubes. *Rev. Adv. Mater. Sci.* **2003**, *4*, 114–122.
19. Scott, J. F. Dimensional Effects on Ferroelectrics: Ultra-Thin Single Crystals, Nanotubes, Nano-Rods, and Nano-Ribbons. *Ferroelectrics* **2005**, *316*, 13–21.
20. Varghese, J.; Whatmore, R. W.; Holmes, J. D. Ferroelectric Nanoparticles, Wires and Tubes: Synthesis, Characterisation and Applications. *J. Mater. Chem. C* **2013**, *1*, 2618–2638.
21. Rørvik, P. M.; Grande, T.; Einarsrud, M. A. One-Dimensional Nanostructures of Ferroelectric Perovskites. *Adv. Mater.* **2011**, *23*, 4007–4034.
22. Shen, B. G.; Sun, J. R.; Xu, F. X.; Zhang, H. W.; Cheng, Z. H. Recent Progress in Exploring Magnetocaloric Materials. *Adv. Mater.* **2009**, *21*, 4545–4564.
23. Smith, A.; Bahl, C.; Bjørk, R.; Engelbrecht, K.; Nielsen, K. K.; Pryds, N. Materials Challenges for High Performance Magnetocaloric Refrigeration Devices. *Adv. Energy Mater.* **2012**, *2*, 1288–1318.
24. Liu, J.; Gottschall, T.; Skokov, K. P.; Moore, J. D.; Gutfleisch, O. Giant Magnetocaloric Effect Driven by Structural Transitions. *Nat. Mater.* **2012**, *11*, 620–626.
25. Zhu, H.; Xiao, C.; Cheng, H.; Grote, F.; Zhang, X.; Yao, T.; Li, Z.; Wang, C.; Wei, S.; Lei, Y.; *et al.* Magnetocaloric Effects in a Freestanding and Flexible Graphene-Based Superlattice Synthesized with a Spatially Confined Reaction. *Nat. Commun.* **2014**, *5*, 3960.
26. Rose, M. C.; Cohen, R. E. Giant Electrocaloric Effect around T_c. *Phys. Rev. Lett.* **2012**, *109*, 187604.
27. Lu, Y.; Claude, J.; Neese, B.; Zhang, Q. M.; Wang, Q. A Modular Approach to Ferroelectric Polymers with Chemically Tunable Curie Temperatures and Dielectric Constants. *J. Am. Chem. Soc.* **2006**, *128*, 8120–8121.
28. Li, Q.; Zhang, G.; Liu, F.; Kuo, H.; Gadinski, M. R.; Xiong, C.; Wang, Q. Solution-Processed Ferroelectric Terpolymer Nanocomposites with High Breakdown Strength and Energy Density Utilizing Boron Nitride Nanosheets. *Energy Environ. Sci.* **2015**, *8*, 922–931.
29. Bao, N.; Shen, L.; Srinivasan, G.; Yanagisawa, K.; Gupta, A. Shape-Controlled Monocrystalline Ferroelectric Barium Titanate Nanostructures: From Nanotubes and Nanowires to Ordered Nanostructures. *J. Phys. Chem. C* **2008**, *112*, 8634–8642.
30. Tang, H.; Zhou, Z.; Sodano, H. A. Relationship between $BaTiO_3$ Nanowire Aspect Ratio and the Dielectric Permittivity of Nanocomposites. *ACS Appl. Mater. Interfaces* **2014**, *6*, 5450–5455.
31. Nelson, J. B.; Riley, D. P. An Experimental Investigation of Extrapolation Methods in The Derivation of Accurate Unit-Cell Dimensions of Crystals. *Proc. Phys. Soc.* **1945**, *57*, 160–176.
32. Tang, H.; Sodano, H. A. Ultra High Energy Density Nanocomposite Capacitors with Fast Discharge Using $Ba_{0.2}Sr_{0.8}TiO_3$ Nanowires. *Nano Lett.* **2013**, *13*, 1373–1379.
33. Abrahams, S. C.; Kurtz, S. K.; Jamieson, P. B. Atomic Displacement Relationship to Curie Temperature and

Spontaneous Polarization in Displacive Ferroelectrics. *Phys. Rev.* **1968**, *172*, 551–553.
34. Choi, K. J.; Biegalski, M.; Li, Y. L.; Sharan, A.; Schubert, J.; Reiche, R.; Chen, Y. B.; Pan, X. Q.; Gopalan, V.; Chen, L. Q.; *et al.* Enhancement of Ferroelectricity in Strained $BaTiO_3$ Thin Films. *Science* **2004**, *306*, 1005–1009.
35. Guo, N.; DiBenedetto, S. A.; Tewari, P.; Lanagan, M. T.; Ratner, M. A.; Marks, T. J. Nanoparticle, Size, Shape, and Interfacial Effects on Leakage Current Density, Permittivity, and Breakdown Strength of Metal Oxide-Polyolefin Nanocomposites: Experiment and Theory. *Chem. Mater.* **2010**, *22*, 1567–1578.
36. Chen, L. Q. Phase-Field Models for Microstructure Evolution. *Annu. Rev. Mater. Res.* **2002**, *32*, 113–140.
37. Chen, L. Q. Phase-Field Method of Phase Transitions/Domain Structures in Ferroelectric Thin Films: A Review. *J. Am. Ceram. Soc.* **2008**, *91*, 1835–1844.
38. Wurfel, P.; Batra, I. P. Depolarization-Field-Induced Instability in Thin Ferroelectric Film-Experiment and Theory. *Phys. Rev. B* **1973**, *8*, 5126–5133.
39. Mehta, R. R.; Siilverman, B. D.; Jacobs, J. T. Depolarization Fields in Thin Ferroelectric Films. *J. Appl. Phys.* **1973**, *44*, 3379–3385.
40. Morozovska, A. N.; Eliseev, E. A.; Glinchuk, M. D. Size Effects and Depolarization Field Influence on the Phase Diagrams of Cylindrical Ferroelectric Nanoparticles. *Phys. B* **2007**, *387*, 358–366.
41. Sharma, A.; Ban, Z. G.; Alpay, S. P.; Mantese, J. V. Pyroelectric Response of Ferroelectric Thin Films. *J. Appl. Phys.* **2004**, *95*, 3618–3625.
42. Wu, C. G.; Li, R. Y.; Zhu, J.; Liu, X. Z.; Zhang, W. L. Great Enhancement of Pyroelectric Properties for $Ba_{0.65}Sr_{0.35}TiO_3$ Films on Pt-Si Substrates by Inserting a Self-Buffered Layer. *J. Appl. Phys.* **2009**, *105*, 044107.
43. Dissado, L. A.; Fothergill, J. C.; Wolfe, S. V.; Hill, R. M. Weibull Statistics in Dielectric Breakdown; Theoretical Basis, Applications and Implications. *IEEE T. Electr. Insul.* **1984**, *EI-19*, 227–233.
44. Ieda, M. Dielectric Breakdown Process of Polymers. *IEEE T. Dielectr. Electr. Insul.* **1980**, *15*, 206–224.
45. Zhang, L.; Wang, Q.; Zhao, X. Mechanical Constraints Enhance Electrical Energy Densities of Soft Dielectrics. *Appl. Phys. Lett.* **2011**, *99*, 171906.
46. Chow, T. S. The Effect of Particle Shape on the Mechanical Properties of Filled Polymers. *J. Mater. Sci.* **1980**, *15*, 1873–1888.
47. Zhang, X.; Chen, W.; Wang, J.; Shen, Y.; Gu, L.; Lin, Y.; C. Nan, C. W. Hierarchical Interfaces Induce High Dielectric Permittivity in Nanocomposites Containing TiO_2@$BaTiO_3$ Nanofibers. *Nanoscale* **2014**, *6*, 6701–6709.
48. Li, X.; Qian, X. S.; Gu, H.; Chen, X.; Lu, S. G.; Lin, M.; Bateman, F.; Zhang, Q. M. *Appl. Phys. Lett.* **2012**, *101*, 132903.
49. Gu, H.; Craven, B.; Qian, X. S.; Li, X.; Cheng, A.; Zhang, Q. M. Simulation of Chip-Size Electrocaloric Refrigerator with High Cooling-Power Density. *Appl. Phys. Lett.* **2013**, *102*, 112901.
50. Correia, T. M.; Young, J. S.; Whatmore, R. W.; Scott, J. F.; Mathur, N. D.; Zhang, Q. Investigation of the electrocaloric effect in a $PbMg_{1/3}Nb_{2/3}O_3$-$PbTiO_3$ relaxor thin film. *Appl. Phys. Lett.* **2009**, *95*, 182904.
51. Wang, Q.; Zhu, L. Polymer Nanocomposites for Electric Energy Storage. *J. Polym. Sci., Part B: Polym. Phys.* **2011**, *49*, 1421–1429.
52. Udayakumar, K. R.; Bart, S. F.; Flynn, A. M.; Chen, J.; Tavrow, L. S.; Cross, L. E.; Brooks, R. A.; Ehrlich, D. J. Ferroelectric Thin Film Ultrasonic Micromotors. In *Proc. of IEEE 4th Int. Workshop on Micro Electro Mechanical Systems (MEMS '91)* Jan 30—Feb 2, 1991, Nara, Japan; IEEE: Piscataway, NJ, **1991**; pp 109—113.
53. Zhang, Q.; Wang, L.; Luo, J.; Tang, Q.; Du, J. Improved Energy Storage Density in Barium Strontium Titanate by Addition of BaO-SiO_2-B_2O_3 Glass. *J. Am. Ceram. Soc.* **2009**, *92*, 1871–1873.
54. Liu, X. Q.; Chen, T. T.; Wu, Y. J.; Chen, X. M. Enhanced Electrocaloric Effects in Spark Plasma-Sintered $Ba_{0.65}Sr_{0.35}TiO_3$-Based Ceramics at Room Temperature. *J. Am. Ceram. Soc.* **2013**, *96*, 1021–1023.
55. Dissado, L. A.; Fothergill, J. C. *Electrical Degradation and Breakdown in Polymers*; Stevens, G. C., Ed.; The Institution of Engineering and Technology: London, 1992; pp 333—335.
56. Li, J. J.; Claude, J.; Norena-Franco, L. E.; Seok, S. I.; Wang, Q. Electrical Energy Storage in Ferroelectric Polymer Nanocomposites Containing Surface-Functionalized $BaTiO_3$ Nanoparticles. *Chem. Mater.* **2008**, *20*, 6304–6306.
57. Li, Y. L.; Hu, S. Y.; Liu, Z. K.; Chen, L. Q. Effect of Electrical Boundary Conditions on Ferroelectric Domain Structures in Thin Films. *Appl. Phys. Lett.* **2002**, *81*, 427–429.
58. Yang, T. N.; Hu, J. M.; Nan, C. W.; Chen, L. Q. Predicting Effective Magnetoelectric Response in Magnetic-Ferroelectric Composites *via* Phase-Field Modeling. *Appl. Phys. Lett.* **2014**, *104*, 052904.
59. Buessem, W. R.; Cross, L. E.; Goswami, A. K. Phenomenological Theory of High Permittivity in Fine-Grained Barium Titanate. *J. Am. Ceram. Soc.* **1966**, *49*, 33–36.
60. Bell, J.; Cross, L. E. A Phenomenological Gibbs Function for $BaTiO_3$ Giving Correct E Field Dependence of All Ferroelectric Phase Changes. *Ferroelectrics* **1984**, *59*, 197–203.
61. Pertsev, N. A.; Tagantsev, A. K.; Setter, N. Phase Transitions and Strain-Induced Ferroelectricity in $SrTiO_3$ Epitaxial Thin Films. *Phys. Rev. B: Condens. Matter Mater. Phys.* **2000**, *61*, R825–R829.
62. Wang, J. J.; Ma, X. Q.; Li, Q.; Britson, J.; Chen, L. Q. Phase Transitions and Domain Structures of Ferroelectric Nanoparticles: Phase Field Model Incorporating Strong Elastic and Dielectric Inhomogeneity. *Acta Mater.* **2013**, *61*, 7591–7603.